Geomechanics and Engineering, *Vol. 28, No. 3 (2022) 265-281*
https://doi.org/10.12989/gae.2022.28.3.265

Experimental and numerical study on the stability of slurry shield tunneling in circular-gravel layer with different cover-span ratios

Xinrong Liu[1,2,3], Dongshuang Liu[1], Fei Xiong*[1], Yafeng Han[1], Ronghan Liu[1], Qingjun Meng[4], Zuliang Zhong[1,2,3], Qiang Chen[1], Chengxian Weng[5] and Wenwu Liu[1]

[1]*School of Civil Engineering, Chongqing University, Chongqing 400045, China*
[2]*State Key Laboratory of Coal Mine Disaster Dynamics and Control, Chongqing University, Chongqing 400044, China*
[3]*National Joint Engineering Research Center of Geohazards Prevention in the Reservoir Areas, Chongqing University, Chongqing 400045, China*
[4]*Nanning Rail Transit Co., Ltd, Nanning, Guangxi, 530029 China*
[5]*T.Y. Lin International Engineering Consulting (China) Co., Ltd, Chongqing 401121, China*

(Received August 28, 2020, Revised December 16, 2021, Accepted December 22, 2021)

Abstract. A set of slurry shield test system capable of cutter cutting and slurry automatic circulation is used to investigate the deformation characteristics, the evolution characteristics of support resistance and the distribution and evolution process of earth pressure during excavating and collapsing of slurry shield tunneling in circular-gravel layer. The influence of cover-span ratio on surface subsidence, support resistance and failure mode of excavation face is also discussed. Three-dimensional numerical calculations are performed to verify the reliability of the test results. The results show that, with the decrease of the supporting force of the excavation face, the surface subsidence goes through four stages: insensitivity, slow growth, rapid growth and stability. The influence of shield excavation on the axial earth pressure of the front soil is greater than that of the vertical earth pressure. When the support resistance of the excavation face decreases to the critical value, the soil in front of the excavation face collapses. The shape of the collapse is similar to that of a bucket. The ultimate support resistance increase with the increase of the cover-span ratio, however, the angle between the bottom of the collapsed body and the direction of the tunnel excavation axis when the excavation face is damaged increase first and then becomes stable. The surface settlement value and the range of settlement trough decrease with the increase of cover-span ratio. The numerical results are basically consistent with the model test results.

Keywords: circular-gravel layer; excavation face stability; model test; numerical simulation; slurry shield

1. Introduction

Underground facilities (i.e., subway tunnel, municipal pipeline, and oil storage tank) are often constructed by shield tunneling method in soft ground (Eskandari 2018, Kim *et al*. 2020, Jeon *et al*. 2020). According to the support type of excavation face, Siegmund Babendererde divides the tunnel excavation machinery into slurry balance shield and earth pressure balance shield (Babendererde 1991). The selection of shield type is closely related to formation permeability and particle composition. In general, when the permeability coefficient of the formation is less than 10^7m s^{-1} or is mainly composed of clay and muddy soil, the earth pressure balance shield can be selected, but when the permeability coefficient of the formation is greater than 10^4m s^{-1} or mainly composed of gravel and coarse sand, the slurry shield should be selected (Editorial Department of China Journal of Highway and Transport 2015). The supporting medium of the excavation face of the slurry shield is fluid, while the supporting medium of the excavation face of the earth pressure balance shield is the excavated material itself. For the slurry shield, the fluid composed of water and additives can be filtered and precipitated on the surface of the excavation face to form an impervious layer. This layer then transfers the pressure of the support fluid to the ground. The stability of the excavation face is always one of the most important aspects in the process of shield tunnel excavation, especially under bad geological conditions (Alagha and Chapman 2019, Zeng *et al.* 2019). Many factors, such as shear strength and permeability of the soil, mud pressure, suspension parameters, tunnel geometric parameter, etc., will affect the stability of the excavation face (Anagnostou and Kovári 1994). In extreme cases, the collapse propagates up to the ground surface creating significant surface subsidence. Therefore, it is necessary to gain a better understanding of the stability of the excavation face of the shield tunnel under bad geological conditions (Zhang *et al*. 2018, Xu and Bezuijen 2019).

The stability of the structure is one of the major issues that designers are concerned about (Han *et al*. 2019, Liu *et al.* 2019, Xue *et al*. 2019). In the past few decades, some scholars have conducted some researches on the stability of slurry shield tunnel excavation (Anagnostou and Kovári 1994, Anagnostou and Kovári 1996, Mansour and Swoboda

*Corresponding author, Ph.D. Student
E-mail: xiongfei@cqu.edu.cn

ISSN: 2005-307X (Print), 2092-6219 (Online)

1997, Broere 1998, Chou *et al*. 2001, Broere and van Tol 2001, Li *et al.* 2009, Zhang *et al.* 2011). Anagnostou and Kovári (1994) and Mansour and Swoboda (1997) studied the relationship between shear strength, the permeability of soil, earth pressure, slurry pressure, suspension parameters, geometric parameters of tunnel and safety factor during slurry shield tunnel excavation. Mansour and Swoboda (1997) also put forward a criterion for identifying the ultimate stable state of shield tunnel excavation face based on the yielding concept. Chou *et al.* (2001) analyzed the stability of the shield tunnel across the liquefiable soil layer, and put forward the anti-liquefaction measures for grouting reinforcement of the liquefiable soil layer. Broere (1998) and Broere and van Tol (2001) proposed an improved method that can be used to calculate the minimum support pressure of slurry shield excavation face in heterogeneous soft soils. Additionally, they found that the influence of horizontal layer boundaries on the support pressure is significant (Broere 1998). Li *et al.* (2009) used the upper bound method of limit analysis and the three-dimensional numerical simulation method to study the stability of slurry shield excavation face in soft clay. Zhang *et al.* (2011) proposed a discrete element numerical method which can simulate the excavating process of the slurry shield. This method is used to analyze the influence of the change of support pressure and buried depth on the stability of the excavation face when the slurry shield tunnel is excavated in soft soil.

The initial researches on slurry shield tunnel mainly focused on the analysis of the influence factors of tunnel stability, control technology and the optimal design of construction parameters (Eisenstein and Ezzeldine 1992, Maid 1992, Uchida *et al.* 1992, Anagnostou and Kovári 1994, Yamaguchi *et al.* 1998, Swoboda and Abu-Krisha 1999, Chou *et al.* 2001). In addition, the initial research methods on the stability of slurry shield tunnel are mainly numerical simulation and theoretical analysis, while the model test method is rarely used (Anagnostou and Kovári 1994, Anagnostou and Kovári 1996, Broere 1998, Broere and van Tol 2001, Li *et al.* 2009, Zhang *et al.* 2011). One of the main reasons is the complexity of the slurry shield test system. However, as an important means to study the mechanical behavior of engineering structures or natural geological bodies, model test plays an important role in revealing the mechanism of phenomena (Smith *et al.* 2016, Wang *et al.* 2018). Therefore, in recent years, a number of scholars have studied the stability (Zizka *et al.* 2019, Huang *et al.* 2020), segment bearing performance (Chaipanna and Jongpradist 2019, Zhang *et al.* 2019), excavation disturbance and surface subsidence (Kim et al. 2018, Park *et al.* 2018, Jallow *et al.* 2019, Naseem *et al.* 2019,) of slurry shield under different geological and construction conditions. At the same time, some test systems which can simulate the main construction process of the slurry shield have been developed one after another (Küpferle *et al.* 2018).

Although the above researches have provided some insights into the stability, construction disturbance, design and construction of slurry shield tunnel, the evolution of support resistance and the mechanical response of soil (deformation characteristics and earth pressure distribution and evolution characteristics) of slurry shield tunnel in the process of excavation and excavation face instability have not been fully explored, especially in circular-gravel layer. The circular gravel layer has strong permeability, which is not conducive to the formation of a stable slurry film on the excavation face, making it difficult to well guarantee the stability of the excavation face. The circular gravel layer is widely seen in southern China, so a slurry shield is frequently used there. This necessitates more in-depth studies on the stability of slurry shield tunnels in the circular-gravel layer. In addition, in most cases, simulation of the excavation face failure process is conducted by removing the excavation face support plate from the slurry shield test equipment (Lv *et al.* 2016, Li *et al.* 2018). There are few slurry shield model test systems that are capable of shield tunneling, slurry circulation and support pressure control of excavation face.

The paper aims to study the stability of slurry shield tunnels in the circular-gravel layer. For this purpose, a slurry shield test system which can realize cutter head cutting and slurry automatic circulation has been developed. A similar material suitable for simulating circular-gravel layer and a slurry material capable of forming a stable permeable slurry film on the excavation face are prepared. Subsequently, the physical model tests with cover-span ratios (calculated from the ground surface to crown of a tuunel) of 0.5, 1.0 and 1.5 were carried out to study the deformation characteristics of circular-gravel layer, the evolution characteristics of support resistance of excavation face and the distribution law and evolution process of earth pressure during excavating and collapsing of slurry shield tunneling in circular-gravel layer. The effects of cover-span ratio on surface subsidence, support resistance and failure mode of excavation face are discussed. In addition, a boundary condition and a three-dimensional numerical model which is basically consistent with the model test are established to verify the reliability of the model test results.

This paper is arranged as follows. The background is stated in Section 2. The developed slurry shield test device and the slurry performance and main test steps are described in Section 3. The deformation characteristics of circular-gravel layer, the evolution characteristics of support resistance and the distribution and evolution process of earth pressure during excavating and collapsing of slurry shield tunneling in circular-gravel layer are analyzed, and the influence of cover-span ratio on surface subsidence, support resistance and failure mode of excavation face are discussed in Section 4. A numerical calculation for verification purposes is performed in Section 5, and the conclusions are drawn in Section 6.

2. Background

The interval of Qingxiushan station-Boyilu station of Nanning Rail Transit Line 3 starts from the north end of Boyi lu station, through Longti Road, Caifeng Road and Yongjiang river to the north bank of Yongjiang river, and then along Qingshan road northbound, finally arrive at Qingxiushan station (Liu *et al*. 2021). The start mileage of

Fig. 1 The location map for the interval of Qingxiushan station-Boyilu station of Nanning Rail Transit Line 3

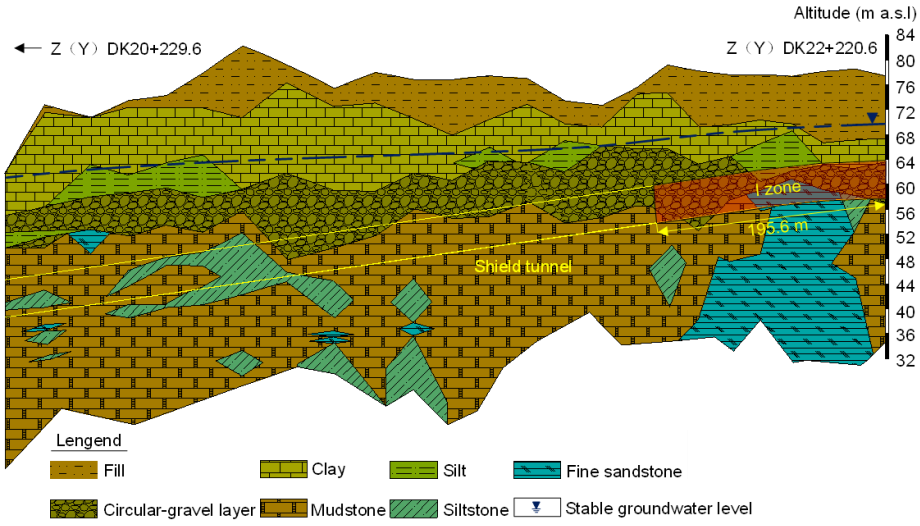

Fig. 2 Stratum information and location of the tunnel (Liu *et al*. 2021)

Table 1 Physical and mechanical parameters of circular-gravel soil and similar materials (Liu *et al*. 2021)

Type	Bulk density (kN/m^3)	Compression modulus (MPa)	Cohesion (kPa)	Internal friction angle (°)	Permeability coefficient (cm/s)
circular-gravel soil	19.9	12.9	0	32.0	3.47×10^{-4}
Similar material	19.9	1.1	0	30.2	9.3×10^{-5}

the interval is Z(Y)DK20+229.6, and the end mileage is Z(Y)DK22+220.6. The tunnel length of the left line is 1987.1 m and the tunnel length of the right line is 1990.8 m. The spacing between tunnels is 10.0~32.7 m. The buried depth of the tunnel is 8.4 to 50.0 m. The tunnel runs under the houses on both sides of Caifeng Road, Nanning Bridge, and the tourist center of the Qingxiu mountain. The project position of this section is shown in Fig. 1.

Two slurry balance shields with a diameter of 6.28 m are used for construction. In the I zone near the end (axis length 195.6 m), a large cross-section of the slurry shield passes through the boulder stratum (See Fig. 2). The circular gravel layer lies below the water table which is mainly composed of boulders, cobble and sand. The majority of the particle size is 2~20 mm, with a few being 30~50 mm. Fig. 3 shows the particle size distribution curve of circular-gravel soil (Liu *et al*. 2021). Table 1 shows the physical and mechanical parameters of circular gravel (Liu *et al*. 2021).

3. Test scheme design

To study on the stability of slurry shield tunneling in circular-gravel layer, a test method similar to the one in previous studies (Liu *et al*. 2021) was employed, which should be described in detail in this paper.

3.1 Determination and calculation of similarity scale

Analog scales are determined by considering field geological conditions, research objectives and performance of testing equipment. The diameter of the model shield

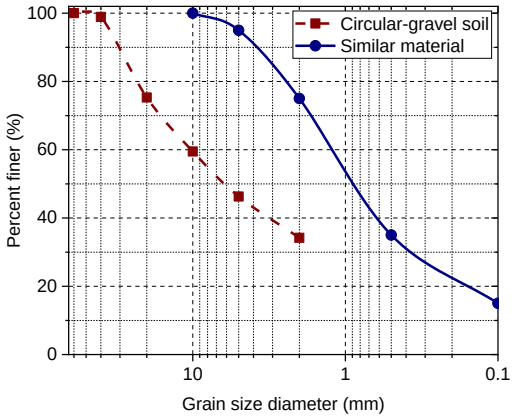

Fig. 3 Particle size distribution curves of circular-gravel soil and similar material (Liu *et al*. 2021)

machine is 500 mm while the slurry balance shields with a diameter of 6.28 m are used for construction in the field, hence, the geometric similarity scale C_L and bulk density similarity scale C_γ of the experimental model is 1/12.56 and 1 respectively. The similarity ratio of the elastic modulus (C_E) is also 1/12.56. Thus, analog scales of other parameters can be deduced according to the analogy theory as follows

$$C_\sigma=C_\delta=C_E=C_c=1/12.56 \quad (1)$$

$$C_\mu=C_\varepsilon=C_\varphi=1 \quad (2)$$

$$C_q=1/3.54 \quad (3)$$

where C_σ is similarity scale of stress; C_δ is similarity scale of displacement; C_E is similarity scale of compression modulus; C_c is similarity scale of cohesion; C_μ is similarity scale of Poisson's ratio; C_ε is similarity scale of strain; C_φ is similarity scale of internal friction angle; C_q is similarity scale of permeability coefficient.

3.2 Similar materials

The mechanical characteristics of strata are the focus of this paper, therefore, the similarity of mechanics and permeability is mainly considered when making similar materials In the experiment, the particle size of the original circular-gravel soil is reduced to obtain the available similar material. Similar soils were obtained through the consolidation tests, direct shear tests and penetration tests (Liu *et al*. 2021). Similar soils are made of gravel of 5~10 mm, fine gravel of 2~5 mm, coarse sand of 0.5~2 mm, medium sand of 0.1~0.5 mm and fine sand < 0.1 mm. Table 1 shows the physical and mechanical parameters of similar materials. Fig. 3 shows the particle size distribution curve of similar materials.

The slurry is mixed with water, bentonite, clay and sodium carboxymethyl cellulose. A total of 9 groups of slurry are mixed. Hydrometer and slurry viscometer are used to determine the density (ρ) and viscosity (v) of slurry at different ratios. The experiment of slurry permeation is carried out by using a self-designed permeation device. Fig. 4 shows the typical slurry film morphology formed after three groups of slurry permeability tests. When the density

(a) (b) (c)

Fig. 4 Typical forms of slurry film. (a) ρ=1.05g/cm^3, v=21s, (b) ρ=1.16g/cm^3, v=31s and (c) ρ=1.24g/cm^3, v=41s (Liu *et al*. 2021)

and viscosity of the slurry are low, the slurry film can not be formed on the surface of similar materials (Fig. 4(a)). When the density and viscosity of the slurry are high, a slurry film of a certain thickness (Figs. 4(b) and 4(c)) can be formed on the surface of similar materials after infiltration, and the thickness of the slurry film increases with the increase of slurry density and viscosity. Considering that the density and viscosity of the slurry used in Fig. 4(b) are close to that of the field (Liu *et al.* 2020), this group of slurry (with ρ=1.16g/cm^3 and v=31s) is used in this model test. The mass ratio of each material in the slurry is water: bentonite: clay: sodium carboxymethyl cellulose = 10: 1: 1.2: 0.008 (Liu *et al*. 2021).

3.3 Testing apparatus

The test is carried out by using a self-designed slurry balance shield test system (Liu *et al*.2021), as shown in Fig. 5. The test system is composed of a model tank, excavation and propulsion system, slurry circulation system and measurement system. The size of the model tank is 1.6 m × 1.4 m × 1.8 m. The model tank is made of a 2 cm thick steel plate. There is a reinforcement beam at the top of the tank to ensure its sufficient stiffness. A 0.8 m × 1.6 m door is placed on the side of the tank to facilitate taking out the similar material after the test. The shield machine model is composed of a guiding cylinder, shield shell, motor and cutter head. The diameter of the model shield machine is 500 mm. Three upper, middle and lower seepage gauges are installed in the slurry chamber and a pressure gauge is installed at the inlet pipe to measure the pressure in the chamber. The slurry chamber is directly connected to the inlet and outlet pipe. The shield machine propulsion system consists of a screw jack and a reaction beam.

A displacement meter is installed on the propulsion system. The displacement meter can collect the advancing distance of the shield machine in real-time. The opening rate of the cutter head is 38%. The slurry circulation system consists of a slurry bucket, a detritus tank and a slurry pump. The slurry is first pumped into the slurry bucket by the slurry pool, and then the grouting pressure is adjusted by adjusting the slurry pressure of the slurry bucket. The composition of the slurry balance shield test system is shown in Fig. 5.

3.4 Data collection

In the process of shield tunneling, the pressure of soil in different directions is measured by earth pressure gauges.

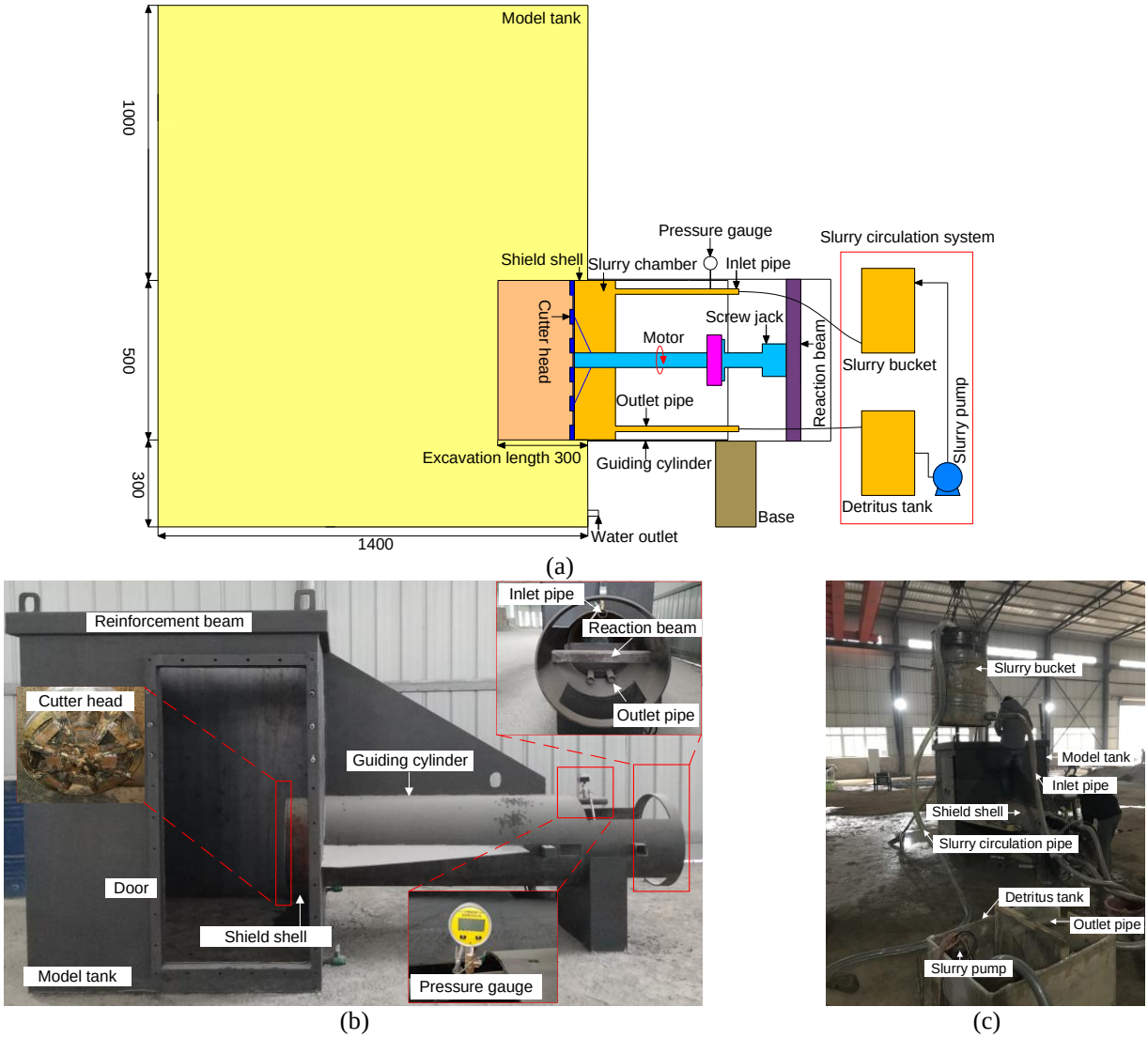

Fig. 5 Test system of slurry balance Shield (unit: mm) (Liu *et al*. 2021). (a) Design drawing, (b) Picture of real object and (c) Slurry circulation system

Fig. 6(a) shows the installation of the earth pressure gauge. Fig. 6(b) shows the installation of the earth pressure gauge in the A-A section. The earth pressure gauges located on the left side of the shield axis are installed perpendicular to the horizontal direction to measure the change of the horizontal pressure of the surrounding soil during excavating. The earth pressure gauges located on the right side of the shield axis are installed perpendicular to the vertical direction to measure the change of the vertical pressure of the surrounding soil during excavating. The earth pressure gauges located in front of the shield axis are installed perpendicular to the vertical direction and perpendicular to the excavation direction. The distance between the two adjacent earth pressure gauges is 50 mm to avoid mutual influence. Fig. 6(c) shows the installation of earth pressure gauges in the B-B section. The earth pressure gauges used in the test are the LY-350 strain type miniature earth pressure gauges, which have a maximum range of 50 kPa, a 0.5 % accuracy, and a working voltage of 2 V.

In the process of excavation, the surface subsidence is measured by a push rod displacement sensor with the models 5G105 and 5G107. The 5G105 sensor has a maximum range of 100mm, a mechanical stroke of 100+3 mm, a precision of 0.01 mm, and a nonlinear error of less than or equal to 0.25%; the 5G107 sensor has a maximum range of 300 mm, a mechanical stroke of 200+3 mm, a precision of 0.01 mm, and a nonlinear error of less than or equal to 0.25%. The above two sensors are operating at 2V. The displacement sensor is fixed on the self-made bracket. Fig. 7(a) shows the installation of the push rod displacement sensor (Liu *et al*. 2021).

The change of slurry pressure in the slurry chamber is measured by the osmometer with a model LY-350 strain-type microseepometer. The osmometer has a range of 0-30 kPa, an accuracy of 0.5%, and a nonlinear error of less than 0.25%. Fig. 7(b) shows the installation of the osmometer (Liu *et al*.2021).

A static strain acquisition instrument with model DH3816N is used to collect the data measured by each

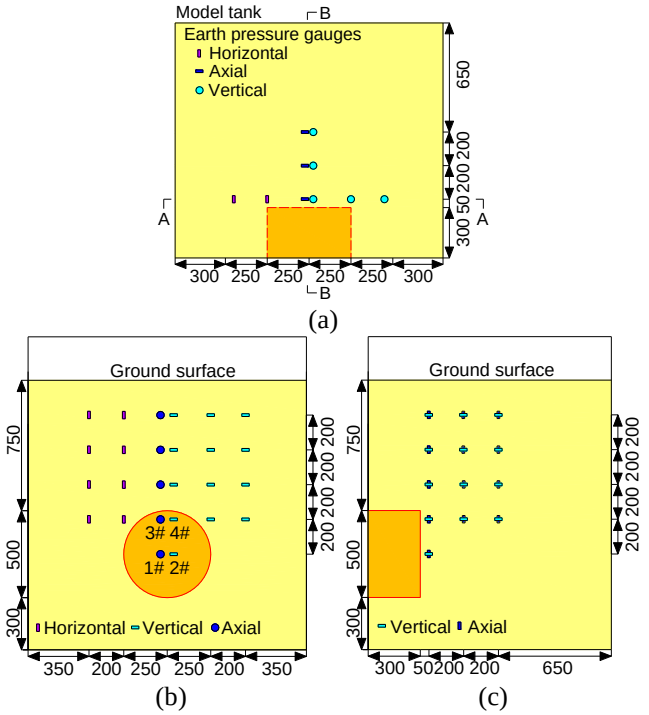

Fig.6 (a) Layout diagram of earth pressure gauge (unit: mm), (b) A-A section and (c) B-B section

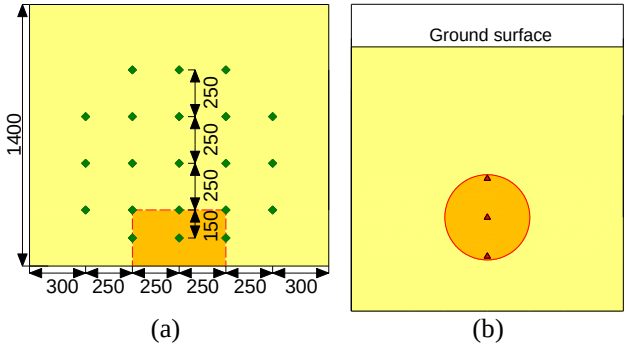

Fig. 7 (a) Push rod displacement sensor (unit: mm); (b) Osmometer (Liu *et al*. 2021)

sensor (Liu *et al*. 2021). It is suitable for measuring strain stress, force, pressure, torque, displacement, temperature, and other physical quantities in model tests. Full bridge, half-bridge, three-wire system 1/4 bridge, and public compensation 1/4 bridge are all supported by the data acquisition instrument, with a bridge voltage of 2 VDC. The strain range is ±60000 με, with a minimum resolution of 0.1 με; the voltage range is 0-2 V, with a minimum resolution of 5 μV. Fig. 8 shows the sensors and acquisition instruments used in the experiment.

3.5 Test procedures

This test is mainly divided into the preparation stage and excavation stage (Fig. 9 and 10 show the main process of physical model testing). The detailed procedures are as follows.

Preparation stage：

(1) Preparation of circular-gravel soil and slurry. The

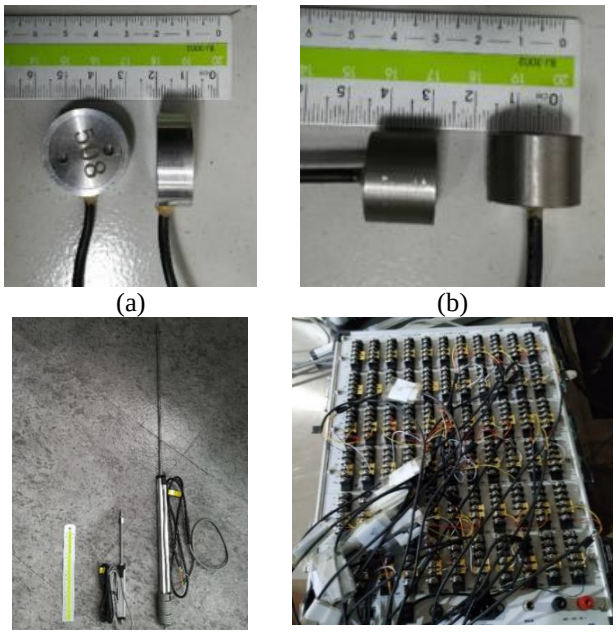

Fig. 8 Sensors and acquisition instruments. (a) Earth pressure gauges, (b) Osmometer, (c) Pull rod displacement sensor and (d) Static strain acquisition instrument

similar soil was proportioned according to the determined ratio and fully stirred. The available slurry was prepared in accordance with the determined ratio and expanded for 16 hours. The CMC was fully dissolved during the extrusion by stirring continuously to achieve the required slurry viscosity.

(2) Filling similar materials. First, a 10 cm high water filter made of gravel with a particle size of 20-50 mm was placed at the bottom of the model tank. Then the model tank was filled with similar soils in layers of 20 cm thickness. After each layer of soil was filled, the soil was tamped by hammering for sufficient compactibility.

(3) Saturating similar materials by hydrostatic saturation method. Each layer of similar soil was fully saturated by hydrostatic saturation. Three layers of iron oxide powder stained soil layer were laid at heights of 55 cm (center plane of shield), 85 cm (5 cm above the shield), and 115 cm.

(4) Installation of measurement sensors. The earth pressure gauges and osmometer were buried and fixed, respectively, according to the instrument's layout diagram. The displacement meter support was installed on the model tank once all of the soil was filled and compacted. Then displacement sensors were mounted on the support, with the end of the sensor ensuring contact with the upper surface of the soil.

Excavation stage

(1) Initial data collection. Collected the initial data from the earth pressure gauges, osmometer, and displacement sensor.

(2) Slurry grouting. Turn on the slurry bucket valve and hoist the slurry bucket to the required height for slurry injection. Turn on the valves on the inlet and outlet slurry pipes, thus the slurry reaches the slurry chamber and form a slurry film on the excavated face. The slurry flowed

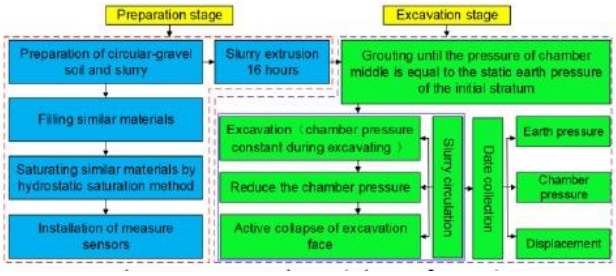

Fig. 9 Test procedures (Liu *et al*. 2021)

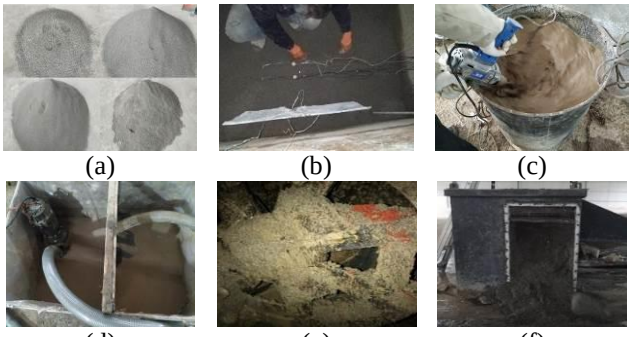

Fig. 10 Test procedures. (a) Soil particle sieving, (b) Model filling and sensor burying, (c) Slurry mixing, (d) Slurry filter residue, (e) Cutter head cutting and (f) Taking out the similar material

smoothly out of the slurry pipe and maintained a constant pressure in the slurry chamber, therefore the system reached a preliminary equilibrium state.

(3) Excavation. After the slurry circulation was stabilized, turn on the shield motor to make the cutter head spiral. The soil was excavated by advancing the shield machine with a constant velocity of 8.8 mm/min, meanwhile, the slurry flow is maintained steadily in this stage.

(4) Slurry circulation was achieved by transporting the filtered slurry from the detritus tank to the slurry bucket by a slurry circulation pump.

(5) Active collapse. First, stopped the shield machine's advance when it reaches 30 cm and keep the cutter head circling and the slurry circulating. Then, reduced the chamber pressure to allow for the active collapse of the excavation face.

4 Results and discussions

4.1 Effect of cover-span ratio on ground surface subsidence

Figs. 11 (a)-11(c) shows the vertical displacement curve of the ground surface above the shield during the test. It can be observed that the ground surface subsidence decreases with the increase of cover-span ratio. For the ground surface displacement, a small uplift will generate in front of the real-time excavation face. When the excavation face is collapsed, a large amount of subsidence occurs on the

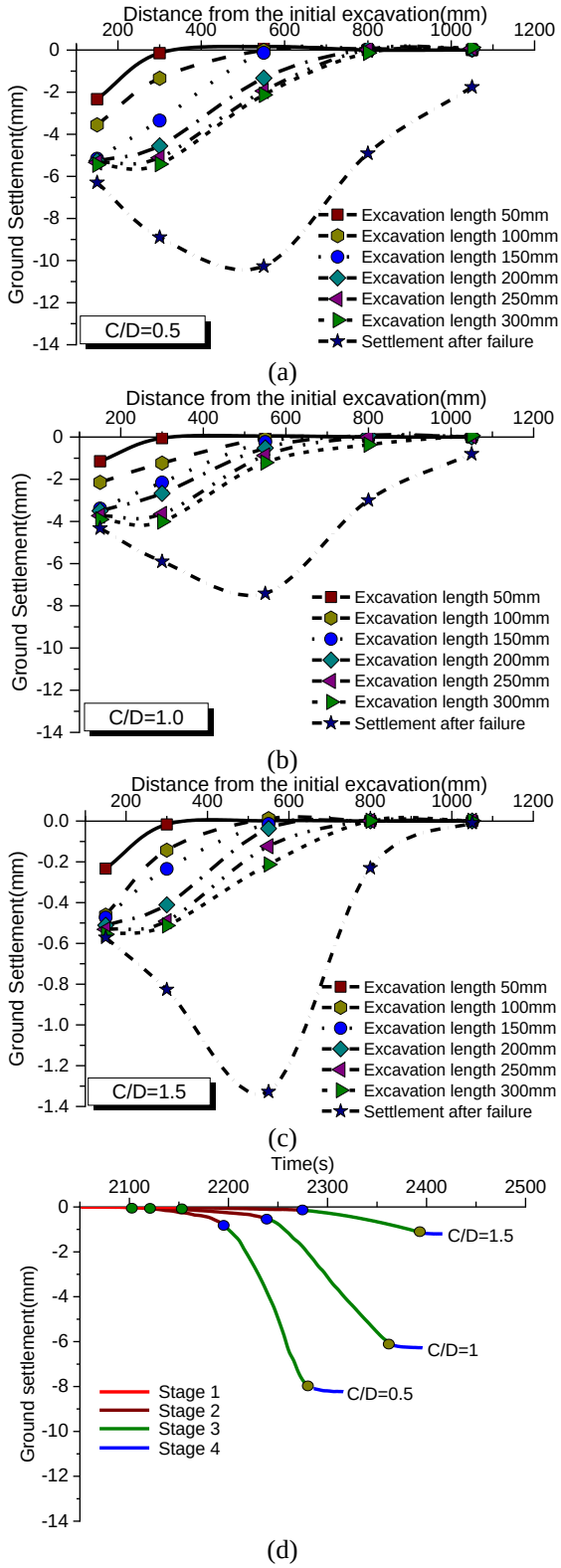

Fig. 11 Variation curves of ground surface displacement under different excavation length. (a) C/D=0.5, (b) C/D=1, (c) C/D=1.5 and (d) Surface subsidence curves in the process of active failure of excavation face

surface. The maximum value of the surface settlement for slurry shield tunneling with the different cover-span ratios is at the position of 0.5D in front of the excavation face.

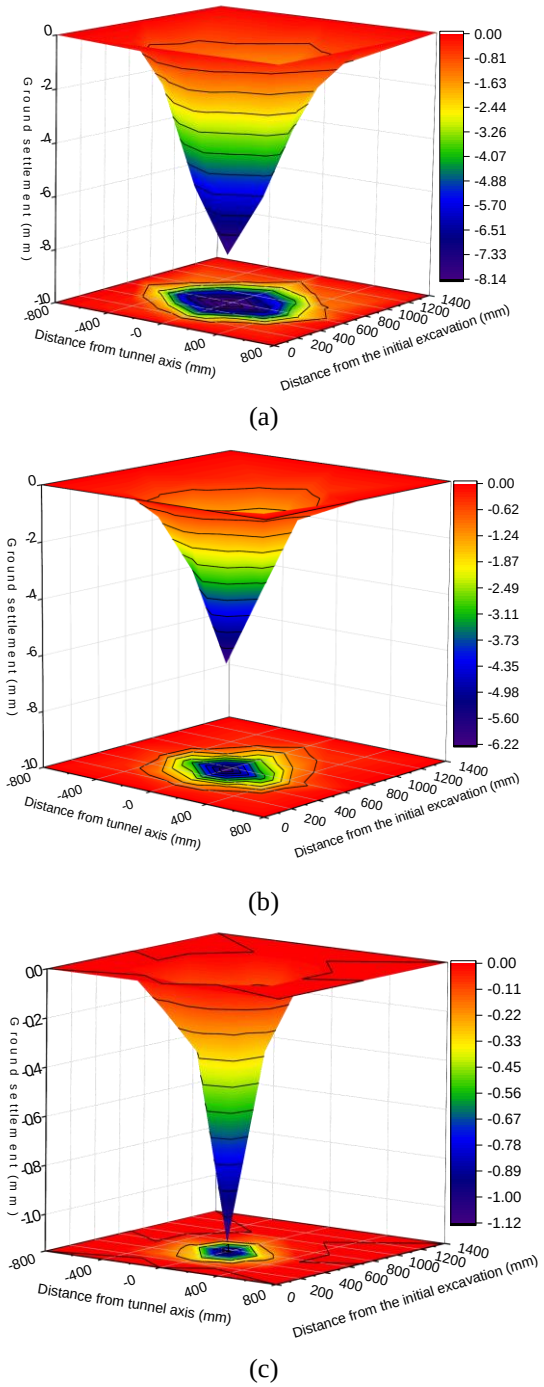

Fig. 12 Contours of final surface settlement; (a) C/D=0.5, (b) C/D=1 and (c) C/D=1.5.

Fig. 11(d) shows the settlement curve of the maximum settlement point of the ground surface during the failure process of the excavation face under different cover-span ratios. According to the characteristics of the curve, the ground surface subsidence in the process of excavation face failure can be divided into four stages.

Insensitivity stage (stage 1). When the shield stops tunneling and reduces the pressure in the slurry chamber, the ground surface subsidence is not sensitive to the decrease of the supporting force of the excavation face, that is, there is only slight or no subsidence on the surface.

Slow-growth stage (stage 2). In the process of supporting resistance gradually approaching the critical value of excavation face failure, the surface subsidence approximately shows a slow linear growth trend. The slope of the settlement curve at this stage is $S_{0.5} > S_1 > S_{1.5}$.

Rapid-growth phase (stage 3). When the support resistance falls below the critical value, the excavation face will be destroyed. The slope of the surface subsidence curve increases, and the growth rate of surface subsidence increases. The order of the slope of the surface subsidence curve at this stage is also $S_{0.5} > S_1 > S_{1.5}$.

Stability stage (stage 4). After the failure of the excavation face, the slope of the settlement curve decreases rapidly. The surface subsidence finally stabilizes at a certain constant value. In the test, it is observed that the soil collapse caused by the failure of the excavation face does not extend to the ground surface. This shows that a certain range of soil arch structure is formed above the collapsed space. The soil arch bears the earth pressure on the upper part of the collapsed space. The ground surface no longer continues to settle. This conclusion will also be verified in later tests.

In addition, the duration of the four stages of surface subsidence varies with the ratio of cover to span. The larger the cover-span ratio is, the later the surface settlement occurs, and the slower the settlement increases. This shows that the larger the cover-span ratio is, the less sensitive the surface subsidence is to the stability of the excavation face. In the other words, when the cover-span ratio is small, that is, the vertical distance between the surface and the excavation face is small, the stratum settlement caused by excavation face failure is easily transmitted to the surface. However, when there is a large cover-span ratio i.e., a large vertical distance between the surface and the excavation face, the stratum settlement caused by the excavation face failure is difficult to transmit to the surface.

Fig. 12 shows the contours of surface subsidence caused by excavation face failure under different cover-span ratios. It can be observed that the smaller the cover-span ratio is, the larger the range of surface subsidence caused by the failure of excavation face is. The point with the maximum subsidence value in the settlement tank appears at 0.5D (D is the shield diameter) in front of the shield excavation face.

4.2 Effect of cover-span ratio on support resistance of the excavation face

Fig. 13 shows the variation curve of the pressure of the slurry chamber during the whole process of the test. The shield machine has a certain effect on the slurry chamber pressure during excavating, so the slurry chamber pressure fluctuates to a small extent (±2 kPa). When the tunneling reaches the final position (300 mm), the grouting pressure begins to decrease and the slurry chamber pressure is also reduced at the same time. When the slurry chamber pressure drops to the limit value P_{min}, damage to the excavation face occurs. Meanwhile, the pressure in the upper, middle and lower parts of the slurry chamber rapidly decreases.

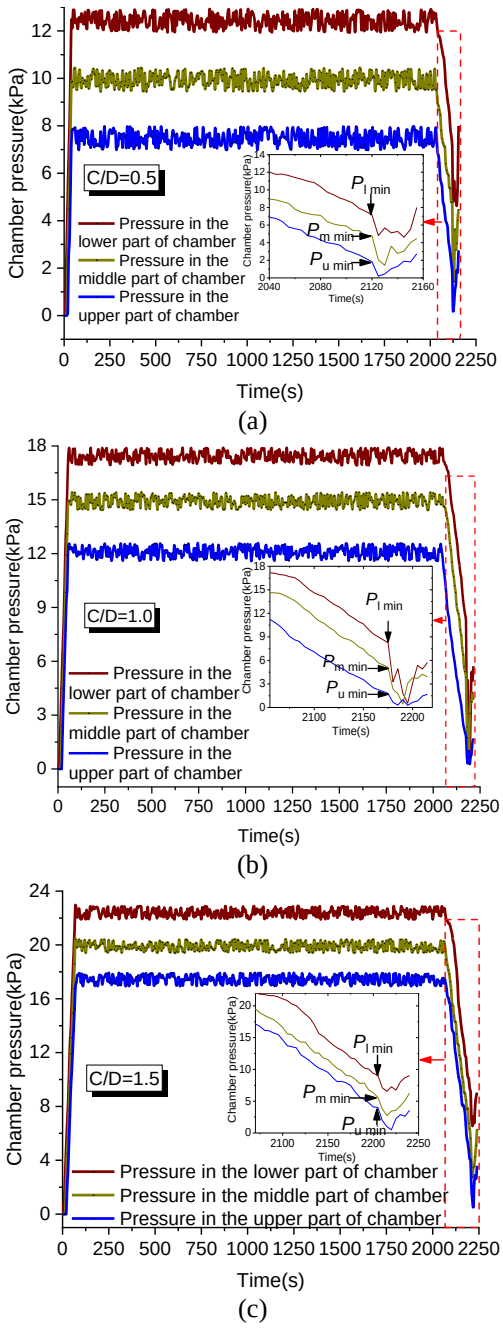

Fig. 13 Variation curves of slurry chamber pressure. (a) C/D=0.5, (b) C/D=1.0 and (c) C/D=1.5.

Subsequently, as the slurry accumulates in the chamber, the chamber pressure rebounds slightly.

The pressure in the middle of the slurry chamber is defined as the ultimate support resistance of the excavation face when the excavation face is damaged. The ultimate support resistance is denoted by P_{usr}. Then it can be inferred that $P_{usr}=P_{m\ min}$. P_{usr} increases with the increase of cover-span ratio, i.e., 4.81 kPa (C/D=0.5), 5.11 kPa (C/D=1) and 5.61 kPa (C/D=1.5), respectively. And with the increase of C/D, the decrease ratio of P_{usr} relative to the initial stable value is greater. The ratio of the ultimate supporting resistance of the excavation face to the stable chamber pressure of the shield tunneling is defined as the ultimate supporting force ratio of the excavation face. The stable chamber pressure (refer to the average value of the pressure in the middle part of the chamber) with different cover-span ratios are 9.95 (C/D=0.5), 14.93 (C/D=1.0) and 19.91 kPa (C/D=1.5), respectively. When C/D is 0.5, 1.0 and 1.5 respectively, the ultimate supporting force ratio of excavation face is 0.48, 0.34 and 0.28 respectively. Obviously, the ultimate supporting force ratio decrease with the increase of the cover-span ratio. Under the same cover-span ratio, the decreasing ratio of chamber pressure in the upper part of the slurry chamber is higher than that in the middle and lower parts. This is because the ultimate supporting force of the excavation face in the slurry shield construction is provided by the slurry chamber pressure, which is an unevenly distributed force. As the pressure gradient of the slurry chamber is different from that of the excavation face, this will lead to a slight difference in the equilibrium state of the upper and lower parts of the excavation face. When the supporting force of the excavation face decreases, the bottom of the excavation face first reaches the limit equilibrium state, while the upper supporting force continues to decrease until the excavation face becomes unstable.

In addition, comparing Fig. 11(d) with Fig. 13, it can be found that the time of active failure of excavation face is basically earlier than that of ground surface subsidence (stage 3), and the time difference increases with the increase of cover-span ratio. This shows that on the one hand, the surface settlement has a certain lag compared with the failure of the excavation face; on the other hand, the increase of the cover-span ratio can facilitate forming a stable soil arch structure above the shield, which will significantly reduce the disturbance to the ground caused by shield excavation.

4.3 Evolution characteristics of earth pressure in front of the excavation face

Taking C/D=1.5 as an example, the variation characteristics of earth pressure in front of the excavation face in the process of shield tunneling are analyzed. Fig. 14 shows the variation curves of earth pressure in front of the excavation face during testing.

In the process of excavation, the soil in front of the excavation face is squeezed, the earth pressure increases, and the growth rate is gradually accelerated. In the descending stage of chamber pressure, the earth pressure in front of the excavation face decreases rapidly, and finally reaches a stable value. During the test, the vertical earth pressure and axial earth pressure variation curve of the B-B section are shown in Fig. 15.

The initial value of vertical earth pressure is the theoretical distributions along with depth due to gravity before tunneling in. It can be observed that with the approach of the shield machine, the soil of the B-B section is squeezed and the vertical pressure increases gradually. When the chamber pressure decreases gradually, the vertical earth pressure increases at first and then decreases along with the buried depth. When the chamber pressure drops to the final value, the earth pressure in front of the excavation

face increases slightly. The vertical earth pressure is basically the same along with the buried depth in the range of 0.75D from the bottom of the shield. The initial value of axial earth pressure in Fig. 15(b) is also the theoretical distribution along with the depth. With the excavation of the shield, the variation characteristics of the axial earth pressure are similar to the vertical earth pressure. However, compared with vertical earth pressure, axial earth pressure is more noticeably affected by the driving process. The increase of axial earth pressure at the centerline of the shield is about 50 %.

From the variation characteristics of vertical and axial earth pressure, it can be seen that when the supporting force of the excavation face decreases to the critical value, the vertical stress of the soil around 0.25D~0.75D above the shield decreases, while the axial stress increases. This shows that the soil arch effect in front of the excavation plays a role. However, the vertical stress and axial stress near the shield excavation face are reduced. This shows that the supporting force of the excavation face decreases, which leads to the collapse of the soil and the stress release of the soil. After the test is stopped, the soil stress gradually stabilizes, and it can be seen that the earth pressure in the stable failure area is basically the same along with the buried depth. In addition, the vertical stress and axial stress more than 1D from the top of the shield are basically consistent with the initial value. This shows that the soil beyond 1D from the excavation site is not disturbed by shield excavation and excavation face failure.

The ratio of axial earth pressure to vertical earth pressure at the same time is defined as the lateral pressure coefficient. The variation curve of the lateral pressure coefficient in the A-A section is shown in Fig. 15(c). The initial value is the coefficient of static earth pressure. In the process of shield tunneling, the lateral pressure coefficient in front of the excavation face decreases gradually from the bottom to the top along with the buried depth. However, when the chamber pressure decreases to a certain value (46 %), the lateral pressure coefficient increases at first and then decreases from the bottom to the top along with the buried depth. Finally, the lateral pressure coefficient in the 0~0.75D region above the shield reaches a stable value, which is close to the active earth pressure coefficient K_a.

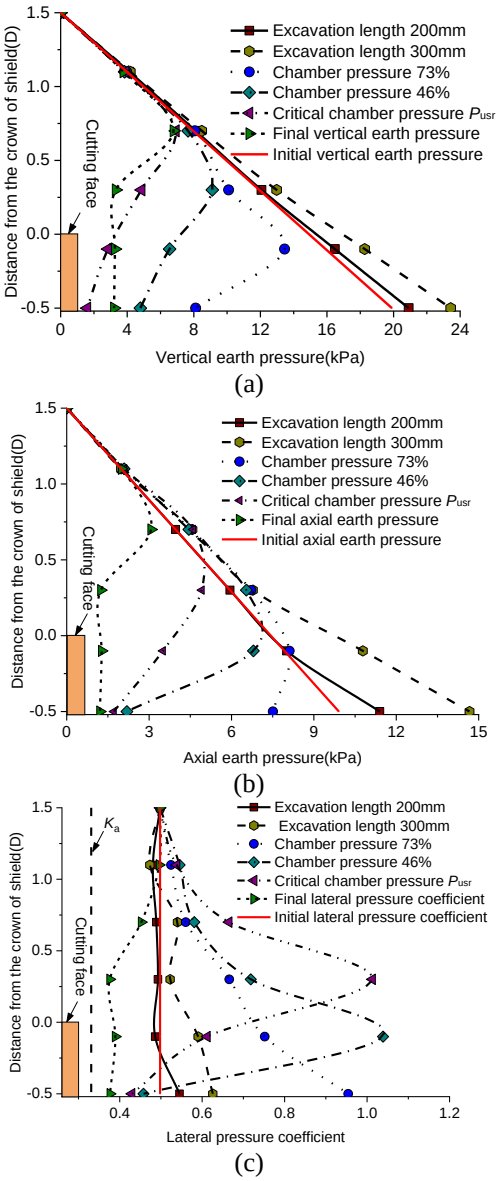

Fig. 15 (a) Variation curves of vertical earth pressure in failure zone, (b) Variation curves of axial earth pressure in failure zone and (c) Variation curves of lateral pressure coefficient in failure zone

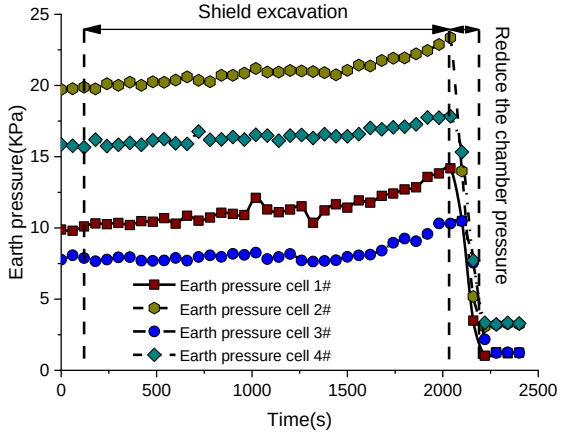

Fig. 14 Variation curves of chamber pressure in front of excavation face during testing

In addition, in the collapse process of the excavation face, a soil arch will be formed on the upper part of the excavation face. The position of the extreme value of each lateral pressure coefficient curve in Fig. 15(c) can be regarded as the vault of the soil arch inside the soil. The extreme value of the lateral pressure coefficient appears at the tunnel crown as the chamber pressure drops to 46%, indicating that the soil arch is formed and the soil arch vault is located at the tunnel crown. However, when the chamber pressure continues to decrease to the critical chamber pressure, the position of the extreme value moves upward to the position of 0.25 D above the tunnel, indicating that the vault of the soil arch also moves upward to this position. To summarize, Fig. 15(c) partially reflects the formation and gradual upward evolution of soil arch in the process of active failure of excavation face.

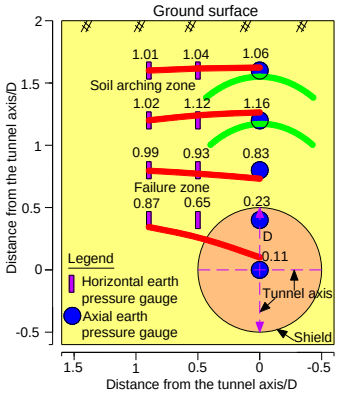

(a)

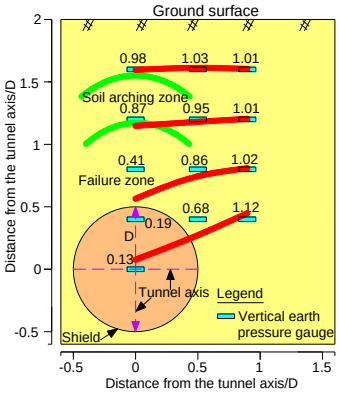

(b)

Fig. 16 Earth pressure coefficient in A-A section; (a) Lateral earth pressure and (b) Vertical earth pressure

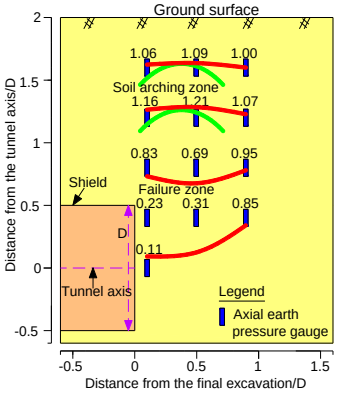

(a)

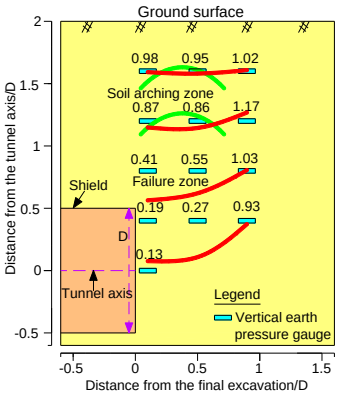

(b)

Fig. 17 Earth pressure coefficient in B-B section; (a) Axial earth pressure and (b) Vertical earth pressure

Figs. 16 and 17 are diagrams of the distribution of earth pressure coefficients in the A-A section and B-B section, respectively. The position of the soil arch in the soil can be preliminarily judged according to Figs. 16 and 17. When the excavation face is under the action of ultimate supporting force, the soil arch is located in the range of 1~1.5D above the center of the shield. In addition, the scope of the horizontal failure area is larger than that of the vertical.

4.4 Failure mode

The excavation faces of the slurry shield tunnelings with different cover-span ratios in the circular-gravel layer show similar failure modes. When the excavation face is damaged, there is a certain settlement on the ground surface, but there are no cracks and holes. The soil mass in the upper front of the shield machine collapses, and the resulting collapse slides into the slurry chamber and forms a slope with a certain inclination (about 60°). At the same time, holes of a certain size are formed in front of the excavation face. Fig. 18 is a diagram of the soil collapse in front of the excavation face under C/D=0.5 in section B-B.

The ratio of the earth pressure (vertical and horizontal) after failure to its initial value is defined as the stress concentration factor to further discuss the evolution process of the failure zone and the final failure mode when the excavation face is in the different support states.

Figs. 19(a) and 19(b) show the evolution process and final failure mode of the failure area in front of the excavation face when the supporting force P is close to and equal to the ultimate supporting force P_{usr}, respectively.

The supporting force of the excavation face is reduced, and the soil in front of the face produces a small uneven displacement. Stress release occurs locally. The vertical and horizontal earth pressure of the soil in this area decrease at the same time, that is, $\lambda_v < 1$, $\lambda_h < 1$, and this area are called the loose area.

Then the soil at the top of the loose area collapses and moves laterally. This will lead to the vertical stress of the soil at the top of the loose area decreases and the horizontal stress increases, that is, $\lambda_v < 1$, $\lambda_h > 1$; meanwhile, the soil adjacent to the loose area is squeezed vertically and loosened horizontally, which results in the decrease of horizontal earth pressure and the increase of vertical earth pressure, which is $\lambda_v > 1$, $\lambda_h < 1$. The vertical earth pressure of the soil above the loose area is less than the horizontal pressure, and the lateral pressure coefficient reaches the maximum, forming a soil arch. Arched feet are formed on both sides. The soil arch is gradually formed (Fig. 19(a). At this point, the soil arch is located deep, and the ground surface settlement is not obvious. When the supporting force decreases to the limit (Fig. 19(b)), the shear failure occurs in front of the excavation face. The distance between the top of the failure area and the excavation face is 0.5D. At this point, the original soil arch at the top of the shield is destroyed. The loose failure surface extends upward and finally achieves a new balance. A new soil arch area is re-formed near the ground surface. The arch height is 1~1.5D.

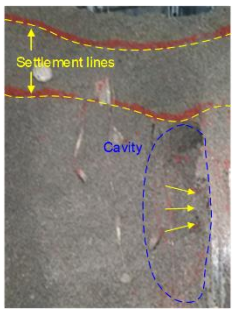

Fig. 18 Typical diagram of the excavation face collapse (in section B-B)

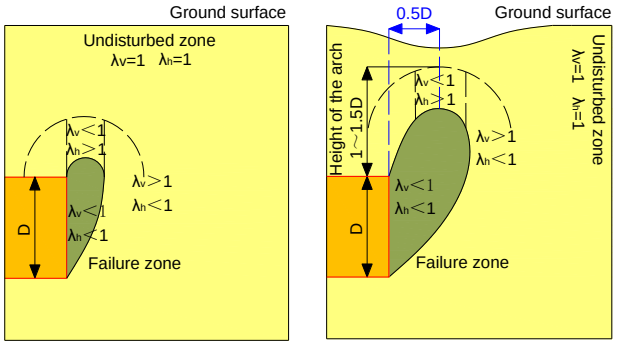

(a) (b)

Fig. 19 Evolution process and failure mode of failure zone under different support conditions. (a) $P > P_{usr}$; (b) $P < P_{usr}$

In this process, significant subsidence will occur on the ground surface.

5. Numerical simulation

5.1 Numerical model and simulation procedures

In order to verify the model test results, and further analyze the mechanical response of the soil in the process of slurry shield tunneling, a numerical study is conducted. The three-dimensional finite difference software FLAC 3D is used to establish a numerical model which is consistent with the size and boundary conditions of the model test. Fig. 20 shows the computational domain of the numerical simulations. Model elements are regular hexahedral elements. The height of the groundwater in the numerical model is the same as that of the ground surface. The diameter of the tunnel in the model is 0.5m. The excavation length is 0.3 m. The left and right boundaries of the model constrained the displacement in the x-direction. The front and rear boundaries constrained the displacement in the y-direction. The bottom boundary constrained the displacement in the z-direction. The top was the free boundary.

After the model is excavated to the design length, the supporting pressure opposite to the original lateral static water pressure and earth pressure is applied on the

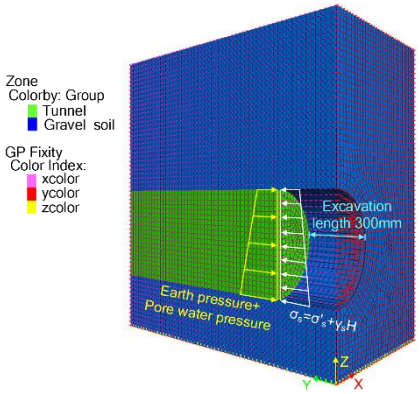

Fig. 20 Numerical model (C/D=1.5)

Table 2 Calculation cases of numerical models with different cover-span ratios

Cover-span ratio	λ'	
	Wide range	The corresponding small range
C/D=0.5	0.1	0.21, 0.22, 0.23, 0.24, 0.25, 0.26, 0.27, 0.28, 0.29
	0.2	
	0.3	
	0.4	
C/D=1.0	0.1	0.11, 0.12, 0.13, 0.14, 0.15, 0.16, 0.17, 0.18, 0.19
	0.2	
	0.3	
	0.4	
C/D=1.5	0.1	0.11, 0.12, 0.13, 0.14, 0.15, 0.16, 0.17, 0.18, 0.19
	0.2	
	0.3	
	0.4	

excavation face. The supporting force σ_s of the excavation face mainly comes from the slurry weight and grouting pressure. In the simulation, the supporting force $\gamma_s H$ on the excavation face produced by the gravity of the slurry itself is applied on the excavation face in the form of linearly decreasing load, while the supporting force σ'_s caused by grouting pressure is applied on the excavation face in the form of uniformly distributed load.

The ratio of the supporting force at the center of the excavation face to the lateral pressure of the original stratum is defined as the supporting ratio $\lambda=\sigma_s/\sigma_o$. The ratio of the supporting force produced by grouting to the grouting pressure needed for the stability of the excavation face during the test is defined as the grouting pressure ratio λ', $\lambda'=\sigma'_s/(\sigma_o-\gamma_s H)$. Fig. 20 shows the numerical model when the ratio of cover to span is C/D=1.5. In the simulation, the mechanical response of the soil around the excavation face and the failure characteristics of the excavation face during the change of grouting pressure ratio are mainly analyzed. The simulation steps are as follows. The mechanical responses of models with different cover-span ratios (i.e., 0.5, 1.0 and 1.5) are first simulated when the grouting

Table 3 Parameters used for numerical modelling

Materials	E(MPa)	μ	c (kPa)	φ (°)	γ(kN/m^3)
Circular-gravel soil	12	0.34	0	30.15	19.9
Shield shell	1.225e5	0.25	-	-	-
Slurry					11.6

pressure ratios (λ') are within the wide range of 0.1-0.4, and the small range in which the limit grouting pressure ratios for the models with different cover-span ratio are located are obtained, and then further simulation is performed on the models with different cover-span ratios under the corresponding small range. Hence, the specific values of the limit grouting pressure ratios for the models with different cover-span ratios can be obtained. Table 2 shows the specific numerical calculation cases under different cover-span ratios.

5.2 Material properties

In the model, the shell element is used to simulate the segment of the shield tunnel. The Mohr–Coulomb constitutive model was adopted for the circular-gravel soil. The parameters used for numerical modeling are presented in Table 3.

5.3 Results analysis

5.3.1 Deformation characteristics of soil

Fig. 21 shows the variation curves of surface vertical displacement and horizontal displacement of excavation face under different grouting pressure ratios. As can be seen, both the vertical displacement of the surface and the horizontal displacement of the excavation face remain unchanged at first, then gradually increase, and finally dramatically increase, as the grouting pressure ratio decreases from 0.4 to 0.1. The vertical displacement of the surface (and horizontal displacement of the excavated face) occur when the grouting pressure ratio drops to a limit value. This value decreases as the cover-span ratio increases, which is consistent with the variation law of the ultimate supporting force ratio obtained in the model tests.

Fig. 22 shows the displacement vector diagram when the soil is in the limit state under different cover-span ratios. It can be seen from the figure that when the supporting force is reduced to a certain extent, a bucket sliding zone extending to the surface will be formed in front of the excavation face. When the cover-span ratio increases from 0.5 to 1.0, The angle between the bottom of the slip zone and the axis of the tunnel increases from 45.2 to 55.0, an increase of 21.68 %. However, as the cover ratio increases from 1.0 to 1.5, the angle increases from 55.0 to 56.0, showing a small change. This angle increases first and then becomes stable with the increase of the cover-span ratio. The slip zone is within the range of 0~1D in front of the excavation face, which is basically consistent with the results of the model test.

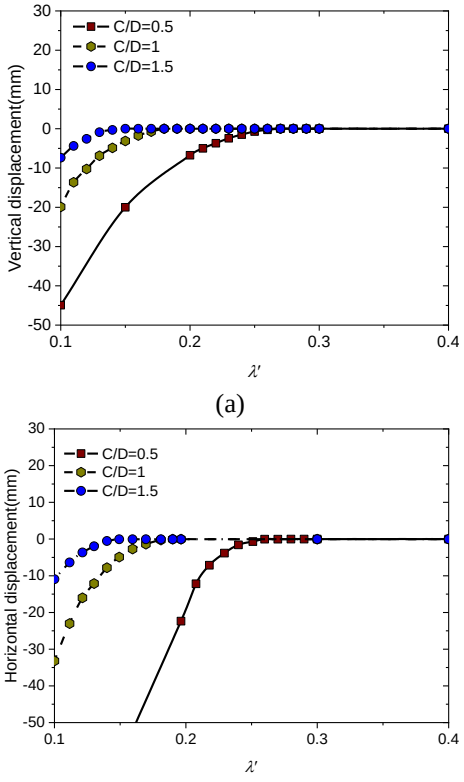

Fig. 21 (a) Relationship between vertical displacement of surface and grouting pressure ratio and (b) Relationship between horizontal displacement of excavation face and grouting pressure ratio

It should be noted that the angles of slip zones in the simulation are smaller than 60º, which was obtained in the physical model (see Section 4.4). There are some differences between numerical simulation and experiment for the following reasons.

(1) The processes of experimental and numerical simulation are distinct. The processes of cutting soil, slurry circulation, slag discharge and shield advance were all replicated in the model tests. After reaching the predetermined excavation distance, stop the shield machine's advance, and reduce chamber pressure so that the excavation face is damaged. At this point, the cutter head keeps rotating and the slurry continues to circulate, and the muck is discharged with the slurry. However, the above process cannot be achieved in numerical simulation. The tunnel is excavated to the preset position in the numerical simulation all at once. After the model is excavated to the design length, the constant supporting pressure opposite to the original lateral static water pressure and earth pressure is applied on the excavation face. Therefore, the realization processes of shield excavation and the failure of excavation face in the model test and numerical simulation are different, which causes the difference between the numerical and experimental results.

(2) After the excavation face is damaged in the model test, the cutter head continues to rotate, the slurry circulates and slurry pressure fluctuates, and the loose muck is still removed from the slurry chamber, which affects the

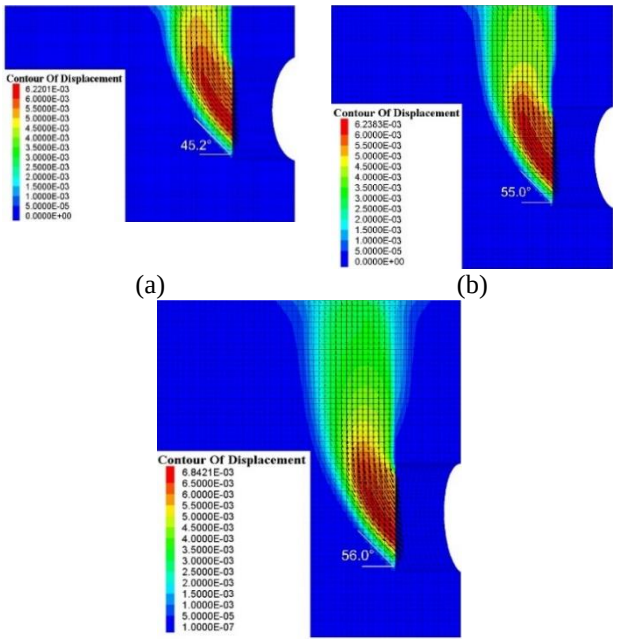

Fig. 22 Displacement vector diagram of slurry shield tunneling with different cover-span ratio in circular-gravel layer. (a) C/D=0.5, (b) C/D=1.0 and (c) C/D=1.5.

deformation and failure of the soil in front of the excavation face. However, numerical simulations are unable to account for the effects of cutter head rotation, slurry pressure fluctuations, and soil loss following the failure of excavation face, resulting in a discrepancy between the numerical and experimental results.

(3) Despite the fact that the mechanical properties of the soil in the model tests and the soil in the numerical simulations are identical, the soil in the model tests is essentially a heterogeneous material, whereas the soil in the numerical simulation is a homogeneous material, which will have an impact on the results.

(4) When observing the failure mode of the excavation face in the model tests, it is necessary to open the side door of the model tank and remove a portion of the soil. One of the reasons for the discrepancy between the experimental and numerical results is that this process will have an impact on the damaged excavation face in the model tests.

For the reasons stated above, some differences between model tests and numerical simulations are inevitable, resulting in a difference between experimental and numerical results. However, the angle between the bottom of the slip zone and the tunnel axis obtained in the experiment is 60°, which is fairly close to the numerical simulation results. It demonstrates that the numerical results are still reliable.

5.3.2 Distribution characteristics of soil stress

Taking the cover-span ratio C/D=1.5 as an example, the vertical stress and horizontal stress isoline of the plane parallel to the axial direction of the shield are extracted when the excavation face is in the limit state, and the isoline of the lateral pressure coefficient of the corresponding plane is also extracted. The distribution characteristics of the soil

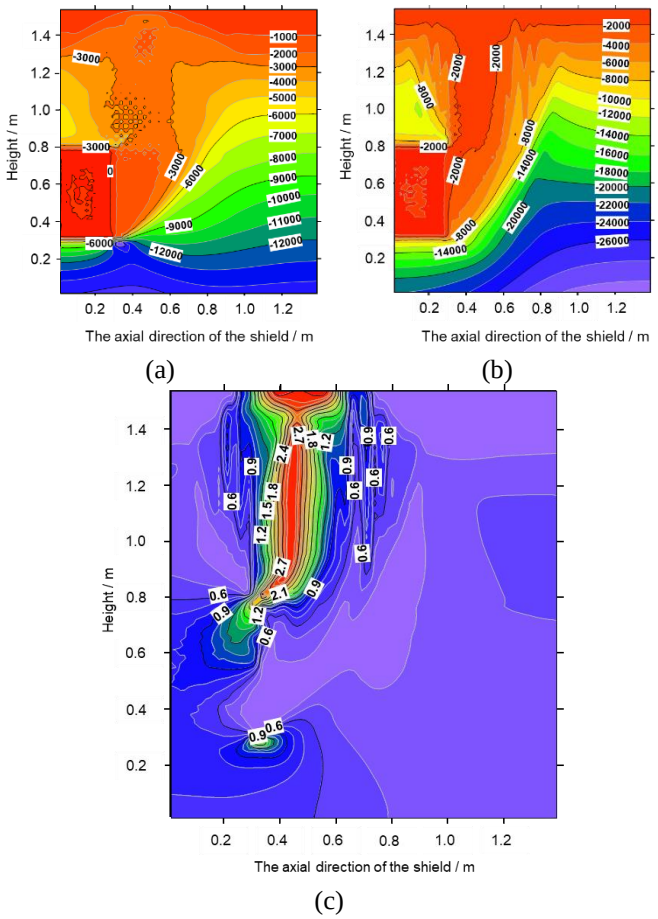

Fig. 23 Stress isoline of the plane parallel to the axial direction of the shield. (a) Horizontal stress (SYY/Pa), (b) Vertical stress (SZZ/Pa) and (c) Lateral pressure coefficient k.

stress field are analyzed when the excavation face is in the limit state. The result is shown in Fig. 23. It can be observed from the diagram that under the condition of the limit state, the vertical stress and horizontal stress in front of the excavation face decrease, and the lateral pressure coefficient increases, with the coefficient sometimes even greater than 1. The maximum lateral pressure coefficient is 2.7.

The ratio of soil stress to initial stress when the excavation face is in the limit state is defined as the stress concentration factor. When the excavation face is in the limit state, the isoline of the stress concentration factor parallel to the axial plane of the shield is extracted, and the result is shown in Fig. 24. It can be seen from the figure that there is an obvious soil arch effect in the soil. The soil arch is located near the surface in front of the excavation face. If the supporting force of the excavation face continues to be reduced, the damage will continue to extend upward to the ground surface, and the soil will be damaged as a whole. The results are consistent with the model test results.

5.3.3 Failure mode

In the simulation, it is found that the shape of the failure body in front of the excavation face of the slurry shield is basically the same under different cover-span ratios. When the support ratio of the excavation face is close to the limit

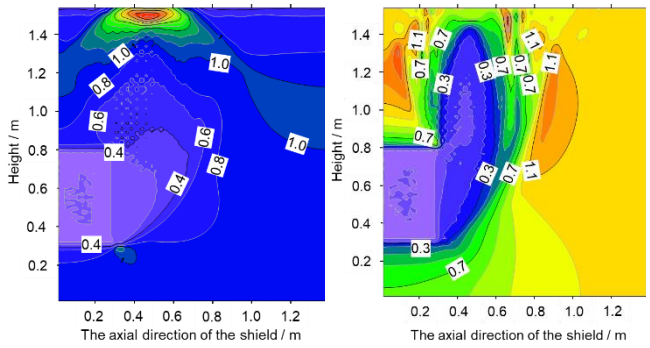

(a) (b)

Fig. 24 The isoline of stress concentration factor of the plane parallel to the axial direction of the shield. (a) horizontal stress ratio and (b) vertical stress ratio

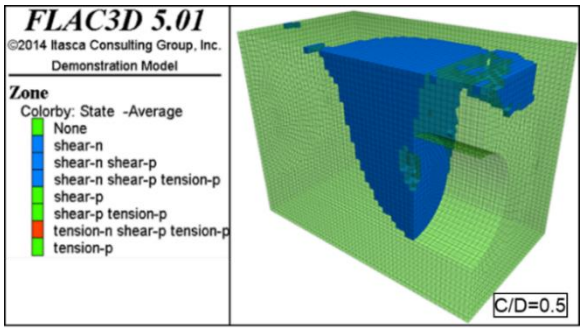

(a)

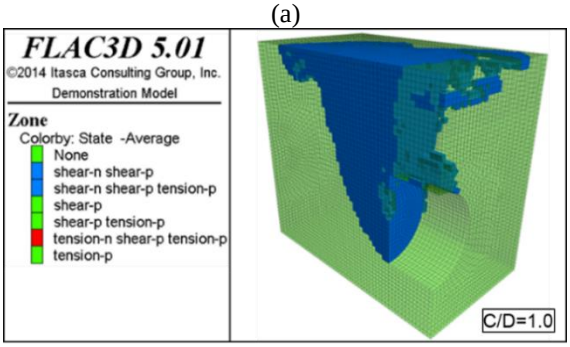

(b)

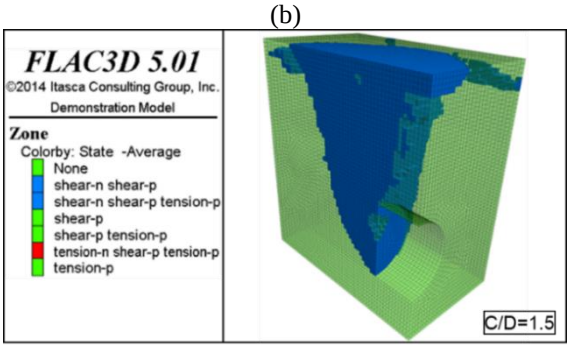

(c)

Fig. 25 Plastic zone distribution of slurry shield tunneling under different cover-span ratio. (a) C/D=0.5, (b) C/D=1 and (c) C/D=1.5

support ratio, the failure area develops rapidly and extends to the ground surface, and finally forms a bucket collapse zone. Fig. 25 shows the plastic zone distribution of slurry shield under different coverage-span ratios. For the slurry shield tunnel with cover-span ratio C/D=0.5, 1.0 and 1.5, the plastic zone completely penetrates and extends to the ground surface when the grouting pressure ratio of the excavation face is reduced to 0.24, 0.16 and 0.12, respectively. The corresponding limit support ratio is 0.46, 0.32 and 0.25, respectively. Obviously, the ultimate support ratio decreases with the increase of the cover-span ratio. This is consistent with the conclusion of the model test. In addition, the limit support ratio obtained by numerical calculation is smaller than that of the model test. This is mainly because the ultimate support ratio in the model test is calculated by the ultimate support force when the soil in front of the excavation collapses, while the limit support ratio in the numerical calculation is calculated by the limit support force when the failure area extends to the surface. Obviously, the supporting force of the former is greater than that of the latter.

6. Conclusions

Using a slurry shield test system, the physical model tests for the stability of slurry shield tunneling under different cover-span ratios are carried out in the circular-gravel stratum. The deformation characteristics of stratum, the evolution characteristics of support resistance and the distribution law and evolution process of earth pressure in the process of excavation and excavation face instability are analyzed, and the influence of cover-span ratio on surface subsidence, support resistance and failure mode of excavation face is discussed. The following conclusions are drawn.

- The surface subsidence decreases with the increase of the cover-span ratio. The larger the cover-span ratio is, the smaller the maximum surface settlement caused by the failure of the excavation face is, and the smaller the range of the settlement tank is. The maximum settlement under different cover-span ratios is at the position of 0.5D in front of the excavation face. With the decrease of the supporting force of the excavation face, the ground surface subsidence goes through four stages: the insensitivity stage, the slow growth stage, the rapid growth stage and the stability stage.
- When the excavation face is damaged, the ultimate support resistance increases with the increase of the cover-span ratio, while the the ultimate supporting force ratio deceases. The surface subsidence has a certain lag compared with the failure of the excavation face, and the time difference increases with the increase of the cover-span ratio.
- In the process of excavation, the soil in front of the shield is squeezed and the earth pressure rises. Compared with the vertical earth pressure, the axial earth pressure is more affected by the excavation process. When the chamber pressure decreases gradually, the vertical earth pressure and axial earth pressure first increase and then decrease along with the buried depth. When the supporting force of the excavation face decreases to the critical value, the soil in a certain range above the shield will produce the soil arch effect, in which the vertical stress decreases

and the axial stress increases, while the soil in front of the excavation surface collapses, and the vertical stress and axial stress near it are reduced.

- After the excavation face is damaged, the soil in the upper front of the excavation face collapses, forming a bucket collapse zone. The shape of the failure body in front of the excavation face of the slurry shield under different cover-span ratios is largely consistent. When the cover span is relatively small (such as C/D=0.5), the soil in the upper front of the excavation face can also form a stable soil arch structure. The soil arch structure can effectively reduce the height of the collapse zone. In addition, the angle between the bottom of the collapse zone and the axis of tunnel excavation increases first and then becomes stable with the increase of cover-span ratio.

Acknowledgments

The research described in this paper was financially supported by the National Key R&D Program of China (Grant No. 2018YFC1504802), National Natural Science Foundation for Young Scientists of China (Grant No. 52104076) and the National Natural Science Foundation of China (Grant No. 52074042).

References

Alagha, A.S.N. and Chapman, D.N. (2019), "Numerical modelling of tunnel face stability in homogeneous and layered soft ground", *Tunn. Undergr. Sp. Tech*., **94**, 103096. https://doi.org/10.1016/j.tust.2019.103096.

Anagnostou, G. and Kovári, K. (1994), "The face stability of slurry-shield-driven tunnels", *Tunn. Undergr. Sp. Tech*.,**9**(2), 165-174. https://doi.org/10.1016/0886-7798(94)90028-0.

Anagnostou, G. and Kovári, K. (1996), "Face stability conditions with earth-pressure-balanced shields", *Tunn. Undergr. Sp. Tech*., **11**(2), 165-173. https://doi.org/10.1016/0886-7798(96)00017-X.

Babendererde, S. (1991), "Tunnelling machines in soft ground: a comparison of slurry and EPB shield systems", *Tunn. Undergr. Sp. Tech*., **6**(2), 169-174. https://doi.org/10.1016/0886-7798(91)90063-A.

Broere, W. (1998), "Face stability calculation for a slurry shield in heterogeneous soft soils", *Proceedings of the World Tunnel Congress 98 on Tunnels and Metropolises*, Sao Paolo, Brazil, April.

Broere, W. and van Tol, A.F. (2001), "Time-dependant infiltration and groundwater flow in a face stability analysis", *Proceedings of the International Symposium on Modern Tunneling Science and Technology*, Kyoto, Japan, October.

Chaipanna, P. and Jongpradist, P. (2019), "3D response analysis of a shield tunnel segmental lining during construction and a parametric study using the ground-spring model", *Tunn. Undergr. Sp. Tech*., **90**, 369-382. https://doi.org/10.1016/j.tust.2019.05.015.

Chou, H.S., Yang, C.Y., Hsieh, B.J. and Chang, S.S. (2001), "A study of liquefaction related damages on shield tunnels", *Tunn. Undergr. Sp. Tech*., **16**(3), 185-193. https://doi.org/10.1016/S0886-7798(01)00057-8.

Editorial Department of China Journal of Highway and Transport. (2015), "Review on China's Tunnel Engineering Research", *Chin. J. Highway Transport*., **28**(5), 1-65. https://doi.org/10.19721/j.cnki.1001-7372.2015.05.001.

Eisenstein, Z. and Ezzeldine, O. (1992), "The effect of tunnelling technology on ground control", *Tunn. Undergr. Sp. Tech*., **7**(3), 273-279. https://doi.org/10.1016/0886-7798(92)90008-6.

Eskandari, F., Goharrizi, K.G. and Hooti, A. (2018), "The impact of EPB pressure on surface settlement and face displacement in intersection of triple tunnels at Mashhad metro", *Geomech. Eng*., **15**(2), 769-774. https://doi.org/10.12989/gae.2018.15.2.769.

Han, Y.F., Liu, X.R., Li, D.L., Tu, Y.L., Deng, Z.Y., Liu, D.S. and Wu, X.C. (2019), "Model test on the bearing behaviors of the tunnel-type anchorage in soft rock with underlying weak interlayers", *B. Eng. Geol. Environ*., **79**(2), 1023-1040. https://doi.org/10.1007/s10064-019-01564-5.

Huang, F., Zhang, M., Wang, F., Ling, T. and Yang, X. (2020), "The failure mechanism of surrounding rock around an existing shield tunnel induced by an adjacent excavation", *Comput. Geotec*., **117**, https://doi.org/10.1016/j.compgeo.2019.103236.

Jeon, Y.J., Jeon, S.C., Jeon, S.J. and Lee, C.J. (2020), "Study on the behaviour of pre-existing single piles to adjacent shield tunnelling by considering the changes in the tunnel face pressures and the locations of the pile tips", *Geomech. Eng*., **21**(2), 187-200. https://doi.org/10.12989/gae.2020.21.2.187.

Jallow, A., Ou, C.Y. and Lim, A. (2019), "Three-dimensional numerical study of long-term settlement induced in shield tunneling", *Tunn. Undergr. Sp. Tech*., **88**, 221-232. https://doi.org/10.1016/j.tust.2019.02.021.

Kim, K., Oh, J., Lee, H., Kim, D. and Choi, H. (2018), "Critical face pressure and backfill pressure in shield TBM tunneling on soft ground", *Geomech. Eng*., **15**(3), 823-831. https://doi.org/10.12989/gae.2018.15.3.823.

Kim, D., Pham, K., Park, S., Oh, J.Y. and Choi, H. (2020), "Determination of effective parameters on surface settlement during shield TBM", *Geomech. Eng*., **21**(2), 153-164. https://doi.org/10.12989/gae.2020.21.2.153.

Küpferle, J., Zizka, Z., Schoesser, B., Röttger, A., Alber, M., Thewes, M. and Theisen, W. (2018), "Influence of the slurry-stabilized tunnel face on shield TBM tool wear regarding the soil mechanical changes-Experimental evidence of changes in the tribological system", *Tunn. Undergr. Sp. Tech*., **74**, 206-216. https://doi.org/10.1016/j.tust.2018.01.011.

Li, Y., Emeriault, F., Kastner, R. and Zhang, Z.X. (2009), "Stability analysis of large slurry shield-driven tunnel in soft clay", *Tunn. Undergr. Sp. Tech*., **24**(4), 472-481. https://doi.org/10.1016/j.tust.2008.10.007.

Liu, X.R., Han, Y.F., Li, D.L., Tu, Y.L., Deng, Z.Y., Yu, C.T. and Wu, X.C. (2019), "Anti-pull mechanisms and weak interlayer parameter sensitivity analysis of tunnel-type anchorages in soft rock with underlying weak interlayers", *Eng. Geol*., **253**, 123-136. https://doi.org/10.1016/j.enggeo.2019.03.012.

Liu, X.R., Xiong, F., Zhou, X.H., Liu, D.S., Chen, Q., Zhang, J.L., Han, Y.F., Xu, B., Deng, Z.Y. and He, C.M. (2021), "Physical model test on the influence of the cutter head opening ratio on slurry shield tunnelling in a cobble layer", *Tunn. Undergr. Sp. Tech*., 104264. https://doi.org/10.1016/j.tust.2021.104264.

Liu, D.S., Liu, X.R., Lin, C.Q., Xiong, F., Han, Y.F., Meng, Q.J., Zhong, Z.L., Chen, Q. and Weng, C.X. (2020), " Experimental study and engineering application of slurry permeability mechanism of slurry shield in circular-gravel stratum", *Arab. J. Geosci*., **13**(9), 1000. https://doi.org/10.1007/s12517-020-05731-x.

Li, J.Y., Liu, W., Zou, J.J., Zhao, Y. and Gong, X.N. (2018), "Large-scale model tests on face instability of shallow shield tunnels in sand", *Chin. J. Geotech. Eng*., **40**(3), 562-567. https://doi.org/10.11779/CJGE201803022.

Lu, X.L., Zhou, Y.C. and Li, F.D. (2016), "Centrifuge model test and numerical simulation of stability of excavation face of shield tunnel in silty sand", *Rock Soil Mech*., **37**(11), 3324-3328.

https://doi.org/10.16285/j.rsm.2016.11.035.
Maid, U. (1992), "Design features of the Botlek rail tunnel in the Betuweroute", *Tunn. Undergr. Sp. Tech*., **14**(2), 135-140. https://doi.org/10.1016/S0886-7798(99)00027-9.
Mansour, M. and Swoboda, G. (1997), "Tunnel face stability of hydroshield tunneling", *Proceedings of the 9th International Conference on Computer Methods and Advances in Geomechanics*, Wuhan, China, November.
Naseem, A., Schotte, K., De Pauw, B. and De Backer, H. (2019), "Ground Settlements due to Construction of Triplet Tunnels with Different Construction Arrangements", *Adv. Civ. Eng*., 1-18. https://doi.org/10.1155/2019/8637837.
Park, H., Oh, J.Y., Kim, D. and Chang, S. (2018), "Monitoring and analysis of ground settlement induced by tunnelling with slurry pressure-balanced tunnel boring machine", *Adv. Civ. Eng*., 1-10. https://doi.org/10.1155/2018/5879402.
Swoboda, G. and Abu-Krisha, A. (1999), "Three-dimensional numerical modelling for TBM tunnelling in consolidated clay", *Tunn. Undergr. Sp. Tech*., **14**(3), 327-333. https://doi.org/10.1016/s0886-7798(99)00047-4.
Smith, A., Dixon, N. and Fowmes, G.J. (2016), "Early detection of first-time slope failures using acoustic emission measurements: large-scale physical modelling", *Géotechnique.*, **67**(2), 138-152. https://doi.org/10.1680/jgeot.15.P.200.
Uchida, K., Wasa, Y. and Kanai, M. (1992), "Design of the shield tunnel for the trans-Tokyo bay highway", *Tunn. Undergr. Sp. Tech*., **7**(3), 251-261. https://doi.org/10.1016/0886-7798(92)90006-4.
Wang, S.G., Liu, Y.R., Tao, Z.F., Zhang, Y., Zhong, D.N., Wu Z.S., Lin, C. and Yang, Q. (2018), "Geomechanical model test for failure and stability analysis of high arch dam based on acoustic emission technique", *Int. J. Rock Mech. Min*., **112**, 95-107. https://doi.org/10.1016/j.ijrmms.2018.10.018.
Xu, T. and Bezuijen, A. (2019), "Experimental study on the mechanisms of bentonite slurry penetration in front of a slurry TBM", *Tunn. Undergr. Sp. Tech*., **93**, 103052. https://doi.org/10.1016/j.tust.2019.103052.
Xue, Y.G., Li, X., Qiu, D.H., Ma, X.M., Kong, F.M., Qu, C.Q. and Zhao, Y. (2019), "Stability evaluation for the excavation face of shield tunnel across the Yangtze River by multi-factor analysis", *Geomech. Eng*., **19**(3), 283-293. https://doi.org/10.12989/gae.2019.19.3.283.
Yamaguchi, I., Yamazaki, I. and Kiritani, Y. (1998), "Study of ground-tunnel interactions of four shield tunnels driven in close proximity, in relation to design and construction of parallel shield tunnels", *Tunn. Undergr. Sp. Tech*., **13**(3), 289-304. https://doi.org/10.1016/S0886-7798(98)00063-7.
Zhang, L., Feng, K., Gou, C., He, C., Liang, K. and Zhang, H. (2019), "Failure tests and bearing performance of prototype segmental linings of shield tunnel under high water pressure", *Tunn. Undergr. Sp. Tech*., **92**, 103053. https://doi.org/10.1016/j.tust.2019.103053.
Zhang, F., Gao, Y., Wu, Y. and Wang, Z. (2018), "Face stability analysis of large-diameter slurry shield-driven tunnels with linearly increasing undrained strength", *Tunn. Undergr. Sp. Tech*., **78**, 178-187. https://doi.org/10.1016/j.tust.2018.04.018.
Zhang, ZX., Hu, X.Y. and Scott, K.D. (2011), "A discrete numerical approach for modeling face stability in slurry shield tunnelling in soft soils", *Comput. Geotech*., **38**(1), 94-104. https://doi.org/10.1016/j.compgeo.2010.10.011.
Zeng, S., Lü, X. and Huang, M. (2019), "Discrete element modeling of static liquefaction of shield tunnel face in saturated sand", *Acta Geotech*., **14**(6), 1643-1652. https://doi.org/10.1007/s11440-019-00806-w.
Zizka, Z., Schoesser, B., Thewes, M. and Schanz, T. (2019), "Slurry shield tunneling: New methodology for simplified prediction of increased pore pressures resulting from slurry infiltration at the tunnel face under cyclic excavation processes", *Int. J. Civ. Eng*., **17**(1), 113-130. https://doi.org/10.1007/s40999-018-0303-2.

CC